

Unique defect structure and advantageous vortex pinning properties in superconducting $\text{CaKFe}_4\text{As}_4$

Shigeyuki Ishida^{1*}, Akira Iyo¹, Hiraku Ogino¹, Hiroshi Eisaki¹, Nao Takeshita¹, Kenji Kawashima², Keiichi Yanagisawa³, Yuuga Kobayashi³, Koji Kimoto³, Hideki Abe³, Motoharu Imai³, Jun-ichi Shimoyama⁴, and Michael Eisterer⁵

¹Electronic and Photonics Research Institute, National Institute of Advanced Industrial Science and Technology, Tsukuba, Ibaraki 305-8568, Japan

²IMRA Materials R&D Co., Ltd., Kariya, Aichi 448-0032, Japan

³National Institute for Materials Science, Tsukuba, Ibaraki 305-0047, Japan

⁴Department of Physics and Mathematics, Aoyama Gakuin University, Sagamihara, Kanagawa 252-5258, Japan

⁵Atominstut, TU Wien, Stadionallee 2, 1020 Vienna, Austria

*corresponding author: s.ishida@aist.go.jp

The lossless current-carrying capacity of a superconductor is limited by its critical current density (J_c). A key to enhance J_c towards real-life applications is engineering defect structures to optimize the pinning landscape. For iron-based superconductors (IBSs) considered as candidate materials for high-field applications, high J_c values have been achieved by various techniques to introduce artificial pinning centres. Here we report extraordinary vortex pinning properties in $\text{CaKFe}_4\text{As}_4$ (CaK1144) arising from the inherent defect structure. Scanning transmission electron microscopy revealed the existence of nanoscale intergrowths of the CaFe_2As_2 phase, which is unique to CaK1144 formed as a line compound. The J_c properties in CaK1144 are found to be distinct from other IBSs characterized by a significant anisotropy with respect to the magnetic field orientation as well as a remarkable pinning mechanism significantly enhanced with increasing temperature. We propose a comprehensive explanation of the J_c properties based on the unique intergrowths acting as pinning centres.

INTRODUCTION

Loss-free electrical transport is a unique property of superconductors that is utilized in various superconductivity applications. The figure of merit for the current-carrying capacity of a superconductor is J_c , which is determined by the material's ability to trap vortices, namely, vortex pinning.¹ Consequently, J_c strongly depends on the defect structure where superconductivity is locally suppressed, and the vortices have smaller energy and are therefore pinned. Thus, how to design and introduce defects is one of the key issues towards real-life applications. To date, various techniques have been developed to control defect structures, particularly through the research on high-transition-temperature (high- T_c) cuprate superconductor $\text{YBa}_2\text{Cu}_3\text{O}_7$ (YBCO) thin films.²⁻⁵ For example, nanoparticles/nanorods can be incorporated by alternately depositing YBCO and a non-superconducting (non-SC) secondary phase (e.g. Y_2BaCuO_5)⁶ or by adding appropriate impurities (e.g. BaZrO_3) to the deposition target.⁷ Moreover, stacking faults and intergrowths (e.g. extra Y or CuO planes) are frequently generated near the inclusions.^{8,9} Additionally, controlled artificial defects can be created by particle irradiation,¹⁰⁻¹² although this technique needs complex and dedicated facilities. In any case, in order to achieve suitable defect structures, the optimization of fabrication conditions such as starting chemical composition, substrate, growth temperature, growing rate, and atmosphere is indispensable, which requires tremendous efforts. Similarly, various techniques have been exploited to introduce artificial defects in iron-based superconductors (IBSs) since their discovery.^{13,14} As in the case of YBCO, J_c has been enhanced particularly for $AE\text{Fe}_2\text{As}_2$ -based (AE : alkaline-earth element) superconductors, the so-called 122 materials, by particle irradiation,¹⁵ addition of BaZrO_3 ,^{16,17} fabrication of superlattices,¹⁸ and introduction of stacking faults.^{19,20} By devising the fabrication process, a significant progress has been achieved in improving J_c of bulks and thin films so far, while further J_c enhancement is required towards real-life applications.

Among the 122 materials, $AE_{1-x}A_x\text{Fe}_2\text{As}_2$ (A : alkali metal element) possesses the highest T_c up to 38 K and largest upper critical fields (H_{c2}) over 100 T with low anisotropy (γ) $\sim 1-2$. These properties are advantageous for high-field applications.²¹⁻²³ In $AE_{1-x}A_x\text{Fe}_2\text{As}_2$ (e.g. $\text{Ba}_{1-x}\text{K}_x\text{Fe}_2\text{As}_2$ (BaK122), Figure 1a), superconductivity is induced by substituting AE with A (hole doping), where AE and A randomly occupy the same crystallographic site in an arbitrary ratio x . Therefore, the superconducting properties, particularly J_c , of $AE_{1-x}A_x\text{Fe}_2\text{As}_2$ significantly depend on x .²⁴ Note that the significant doping dependence of J_c is common to other 122 materials with different dopant elements.²⁵⁻²⁷ As a result, a fine adjustment of x is required to achieve better properties of bulks and thin films. In this study, we focus on the recently discovered 1144 materials,^{28,29} $AE\text{AFe}_4\text{As}_4$, which possess T_c and H_{c2} comparable to 122 materials. In the 1144 structure (Figure 1b), AE and A do not occupy the same site owing to the large difference in the ionic radii (e.g. 1.21 Å and 1.51 Å for Ca^{2+} and K^+ , respectively); hence, AE and A layers stack alternately along the c axis. Therefore, the 1144 material is a line compound where the Fe valence state is fixed at 2.25+. This characteristic is advantageous for applications because fluctuations in chemical composition is, in principle, not allowed. Meanwhile, for such an ordered-layered structure, 122 phases ($AE122$ and $A122$) intergrow in the CaK1144 matrix if excess of AE or A prevails during the synthesis process. Since $AE122$ are non-SC parent materials and $A122$ are superconductors with low $T_c < 4$ K (practically non-SC), such intergrowths possibly act as vortex-pinning centres. In fact, recent studies on vortex pinning properties of CaK1144 reported unusually high J_c ³⁰ as well as vortex dynamics distinct from 122 materials,³¹ while the relevant pinning mechanisms remain unsolved. This motivated us to explore the microstructure and the vortex pinning mechanisms in CaK1144 . Here we demonstrate the unique defect

structure in CaK1144, which provides comprehensive explanations of the sublime vortex pinning properties.

RESULTS

Microstructure of CaKFe₄As₄ single crystal

The crystal structure of the CaK1144 matrix and the unique defect structure can be directly observed by high-resolution scanning transmission electron microscopy (STEM) experiments. Figure 1c shows a low-magnification annular-dark-field (ADF)-STEM image taken along the [100] axis. Overall, the STEM image shows a uniform contrast, indicative of good homogeneity of the matrix region. Notably, characteristic bright stripes in the horizontal direction with typical lengths of $\sim 1 \mu\text{m}$ can be identified. These structures are regarded as planar defects along the ab plane, while no other defects are detected. Figure 1d shows the ADF-STEM image around one of the bright stripes. The upper right panel shows the magnified view of the CaK1144 matrix. The brightest zig-zag arrangements of dumbbells indicated by green arrows are assigned to FeAs layers. The Fe-Fe interplane distance across the two kinds of relatively dark layers (the brighter and the darker ones indicated by blue and orange arrows, respectively) was determined to be 6.1 \AA and 7.0 \AA , respectively. These values are in good agreement with the reported ones (6.12 \AA and 6.70 \AA , see Figure 1b), indicating that the brighter and darker layers correspond to Ca and K layers, respectively. Thus, we confirmed that the alternating stacking of Ca and K layers is indeed realized in the matrix.

Next, we focus on the bright stripe magnified in the right lower panel in Figure 1d. It reveals that the alternation of Ca and K layers is violated, while the local FeAs-layer structure is maintained. There are nine FeAs-to-FeAs units with a total thickness of about 55 \AA , and each Fe-Fe interplane distance is found to be 6.1 \AA , which is identical to that across the Ca layer. The chemical composition analysis shows that Ca is rich around the defect without significant changes for Fe and As (see Supplementary information). Based on the results, we conclude that the defect is a Ca122 intergrowth with dimensions of $\sim 5.5 \text{ nm}$ (~ 5 unit cells) along the c axis and $\sim 1 \mu\text{m}$ along the ab -plane, which is coherently grown in the CaK1144 matrix.

Furthermore, when the microstructure of CaK1144 was carefully investigated, we found much smaller defects. In Figure 1e, there is a thin bright line indicated by a black arrow. This defect is identified to be a monolayer Ca122 intergrowth, as shown in the right panel. Typically, such thin intergrowths have dimensions of 1–2 nm in thickness (along the c -axis) and 50–100 nm in length (along the ab -planes). Thus, the existence of Ca122 intergrowths with various sizes is revealed. Such intergrowths should have significant influence on the vortex pinning properties in CaK1144.

Critical current properties in CaKFe₄As₄

Magnetization hysteresis loops (MHLs) were investigated ($M \sim J_c$) in order to explore the vortex pinning properties in CaK1144. First, MHLs with H parallel to the c -axis are shown (Figures 2a and 2b), which have been intensively investigated to evaluate the in-plane J_c for $H \parallel c$ ($J_c^{H \parallel c}$) in the IBSs. Each MHL shows a peak around self-field ($H = 0$) commonly seen for other IBSs. The H dependence of $J_c^{H \parallel c}$ calculated from the MHLs is shown in Figure 2c. Surprisingly, $J_c^{H \parallel c}$ increases with increasing temperature (T) in the high H region, which is contrary to the common knowledge about the T dependence of J_c . For example, $J_c^{H \parallel c}$ at $T = 3 \text{ K}$ (black) and that at $T = 20 \text{ K}$ (light blue) cross each other at around $\mu_0 H \sim 4 \text{ T}$, resulting in a larger $J_c^{H \parallel c}$ for $T = 20 \text{ K}$ in a high H region. The feature is clearly seen

in the T dependence of $J_c^{H//c}$ ($J_c^{H//c} - T$ at 0.4, 1, 3, and 6 T) plotted in Figure 2d, showing a broad peak at around 20 K under various H . Under the low H below 1 T, the peak in $J_c^{H//c} - T$ is absent since J_c at low T is dominated by the strong pinning contribution (corresponding to the peak around $H=0$) arising from sparse and large pointlike defects³² (see the Supplementary information). To our knowledge, such a large increase in J_c with increasing T in wide T and H ranges has not been reported previously in other IBSs nor high- T_c cuprates (note that there are several examples of increase in J_c with increasing T , while they are in general accompanied by a prominent second magnetization peak in MHLs²⁷ in contrast to the present moderate H dependence of J_c). The unusual T dependence of J_c , namely, the “peak effect” in $J_c - T$, highlights a remarkable enhancement of pinning with increasing T even at temperatures well below T_c , which is unique to CaK1144. It is evident that the T dependence of $J_c^{H//c}$ of CaK1144 is distinct from that of the 122 materials. In Figure 2e, the T dependence of $J_c^{H//c}$ at 6 T for CaK1144 is compared with those for various 122 materials²⁷; $\text{Ba}_{1-x}\text{K}_x\text{Fe}_2\text{As}_2$, $\text{Ba}(\text{Fe}_{1-x}\text{Co}_x)_2\text{As}_2$, and $\text{BaFe}_2(\text{As}_{1-x}\text{P}_x)_2$ with different x values. Although $J_c^{H//c}$ of CaK1144 is relatively small at low T , the maximum $J_c^{H//c} = 0.17$ MA/cm² at 20 K is comparable to the highest one reported for 122 materials. Such high J_c demonstrates that the T -enhanced pinning centres trap vortices very efficiently.

Next, we show MHLs with H along the ab plane to evaluate J_c for $H // ab$ ($J_c^{H//ab}$). Figure 3a shows the MHLs for CaK1144. The shape of the MHL is clearly different from that for $H // c$ in that it shows a dip structure around self-field, which will be discussed later. Moreover, the size of the MHL monotonically decreases with increasing T in contrast to the case of $H // c$, suggesting a significant anisotropy in the vortex pinning properties with respect to the H orientation. Figure 3b shows the H dependence of $J_c^{H//ab}$ derived from the MHLs. Here, we applied a simplified calculation procedure following the previous work³⁰ (see Methods and Supplementary information). The estimated $J_c^{H//ab}$ is extremely large, 5 MA/cm² at 5 K and 3 T, which is ~ 40 times larger than $J_c^{H//c}$. $J_c^{H//ab}$ maintains large values at higher T , over 1 MA/cm² up to 6 T at 20 K and up to 3 T at 25 K. These values are comparable with the highest J_c in IBS thin films^{20,33} (see Figure 3e).

The unusually high $J_c^{H//ab}$ in CaK1144 can be confirmed by comparing with the results of BaK122 obtained by the same procedure. Figure 3c shows the MHLs for BaK122 ($x = 0.4$). In contrast to the case of CaK1144, the MHLs show a peak around self-field, similar to that for $H // c$. Figure 3d shows the H dependence of $J_c^{H//ab}$ for BaK122. Notably, $J_c^{H//ab}$ of BaK122 is much smaller than that estimated for CaK1144. For example, $J_c^{H//ab} = 0.3$ MA/cm² at 5 K and 3 T is smaller by one order of magnitude and 0.01 MA/cm² at 25 K is smaller by two orders. Such a large difference supports the high J_c arising from a unique pinning mechanism in CaK1144.

Figures 3e and 3f show the T dependences of $J_c^{H//ab}$ (filled circles), $J_c^{H//c}$ (open circles), and the J_c anisotropy defined as $J_c^{H//ab}/J_c^{H//c}$ (stars) for CaK1144 (red symbols) and BaK122 (blue symbols), respectively. $J_c^{H//ab}$ and $J_c^{H//c}$ of Co-Ba122²⁰ and NdFeAs(O,F)³³ (Nd1111) thin films are plotted for comparison. In the case of CaK1144, the pinning is significantly anisotropic with respect to the H orientation, as demonstrated by the distinct magnitude as well as the T dependence of J_c for $H // ab$ and c . The anisotropy tends to increase with decreasing T , taking a maximum value of ~ 40 around 5–7 K. At higher $T > 10$ K, where $J_c^{H//c}$ increases, the anisotropy decreases to ~ 10 at 20 K. In contrast, for BaK122, $J_c^{H//ab}$ and $J_c^{H//c}$ almost overlap each other, i.e. J_c is isotropic at T below 20 K. Moreover, the anisotropy increases with T in contrast to the case of CaK1144. Apparently, the T dependence of J_c anisotropy of BaK122 is similar to that of H_{c2} anisotropy.^{34,35} Such a correlation between the J_c anisotropy and the H_{c2} anisotropy

can be qualitatively understood in terms of the anisotropy of coherence length (ξ) together with pinning by random point defects³. Thus, in the case of BaK122, common pinning centres likely dominate J_c both for $H // ab$ and c .

DISCUSSION

The extraordinary vortex pinning properties in CaK1144 are summarized as follows; (i) $J_c^{H//c} - T$ shows an unexpected peak effect and (ii) $J_c^{H//ab}$ is unusually large. Regarding $H // c$, the H and T dependence of $J_c^{H//c}$ of CaK1144 is visualized in the form of a contour plot in Figure 4a. Several characteristic T and H corresponding to the two types of peak effect observed in $J_c^{H//c} - T$ and MHLs are also marked. For comparison, the corresponding data for BaK122 ($x = 0.3$) which possesses the highest J_c among the 122 materials²⁷ are shown in Figure 4b. The colour distribution for CaK1144 is characterized by the hot-colour region in the intermediate T range. It is found that the peak in $J_c^{H//c} - T$ (T_p) is almost H -independent, suggestive of a unique origin of the enhanced pinning with increasing T . At high T region (approximately above T_p), the peak in MHLs (H_p) appears in the observable H range (< 7 T) similarly to BaK122, which is in general associated with the order-disorder transition of the vortex lattice. It is evident that T_p and H_p are well-separated in the $H - T$ phase diagram, suggestive of the different mechanisms underlying the two types of peak effect.

Now we return to the defect structure in CaK1144 to understand the anomalous J_c properties. The Ca122 intergrowths observed by the STEM are schematized in Figures 1f and 1g. The colour gradation indicates the difference in T_c between the matrix and the defects. The intergrowths are considered to be categorized into two types; (i) intergrowths which are thick (5–10 nm) along c axis and large ($\sim 1 \mu\text{m}$) along the ab plane (Figure 1f), and (ii) thin (1–2 nm) and small (~ 100 nm) ones (Figure 1g). For the former case, the thickness is typically ~ 5 nm, as represented by Figure 1d, which is much larger than the c -axis coherence length ($\xi_c \sim 1$ nm)³⁶ of CaK1144. Such intergrowths are regarded as non-SC planar defects because the inner part of the intergrowths is considered to be undoped Ca122. In general, these defects act as efficient pinning centres for $H // ab$ while they do not contribute to pinning for $H // c$. On the other hand, for the latter case, when the thickness is ~ 1 –2 nm, i.e. 1-2 Ca layers are inserted (Figure 1e), holes can be supplied to the inner FeAs layers from the K layers, hence such intergrowths are considered to be SC defects. It is expected that T_c of the SC defects (T_c^{defect}) is lower than that of the CaK1144 matrix due to the depleted carrier density as in the case of underdoped BaK122. Then, T_c^{defect} is determined by the number of Ca layers in the defect, hence it likely takes discrete values. In addition, these defects terminate in a short range ($< \sim 100$ nm); hence, T_c abruptly changes along the ab plane around their ends. Therefore, they act as effective pinning centres not only for $H // ab$ but also for $H // c$.

Among those two types of defects, the former one is considered to give rise to the unusually large $J_c^{H//ab}$ as well as J_c anisotropy as in the case of artificial superlattices in thin films. In addition, such defects can account for the dip feature in the MHLs, which has been reported for irradiated IBSs where J_c is significantly enhanced. For the dip feature, two explanations have been considered: a highly inhomogeneous field distribution³⁷ and the anisotropy of J_c .³⁸ Both are compatible with the properties of CaK1144. The self-field is in general inhomogeneous with strongly curved flux lines, hence the local field can not be parallel to the intergrowths in the entire sample, and thus pinning by the intergrowths is less effective at low fields. Meanwhile, the intergrowths can cause the large J_c anisotropy ($J_c^{H//ab} \gg J_c^{H//c}$ as well as the inter-/intra-plane J_c anisotropy).

On the other hand, the latter type is considered to play a key role in the unusual T dependence of $J_c^{H//c}$. The strength of pinning around the ends of the intergrowths is determined by the difference in condensation energy between the matrix and defects ($\Delta E_c = E_c^{1144} - E_c^{\text{defect}}$). The condensation energy ($E_c = H_c^2/8\pi$ where H_c is thermodynamic critical field), which is the difference of the ground state energies between the normal state and the SC state, depends on T . Because the thin intergrowths are superconducting at low T ($E_c^{\text{defect}} > 0$), ΔE_c is likely small hence the pinning is weak. When the intergrowths turn into the normal state ($E_c^{\text{defect}} = 0$) with increasing T , the pinning becomes stronger owing to the larger energy gain. Thus, the thin intergrowths, i.e. the SC defects, are regarded as T -enhanced pinning centres, which possibly give rise to the increase in $J_c^{H//c}$ with increasing T .

To our knowledge, the idea of SC defects has been well-known, while the T dependence of J_c in the presence of SC defects has not been sufficiently investigated. Here, we calculate the pinning force density f_p using a simple model; $f_p \sim \Delta E_c \xi$ where $\Delta E_c = E_c^{1144} - E_c^{\text{defect}}$ is the difference in E_c between CaK1144 matrix and SC defect ($\Delta E_c > 0$ considering $T_c^{\text{defect}} < T_c^{1144}$), and ξ is the coherence length. Here, the T dependences of E_c and ξ are modelled by $E_c \sim H_c^2 \sim [1 - (T/T_c)^2]^2$ and $\xi \sim [(1 + (T/T_c)^2)/(1 - (T/T_c)^2)]^{1/2}$, respectively. First, in the case of non-SC defects where $T_c^{\text{defect}} = 0$ and $E_c^{\text{defect}} = 0$ (i.e. $\Delta E_c = E_c^{1144}$), f_p ($\sim E_c^{1144} \xi$) monotonically decreases with increasing T (Figure 5a). Next, an example result for SC defects is shown in Figure 5b. Here, $T_c^{\text{defect}} = 25$ K (corresponding to underdoped BaK122 with $x \sim 0.25$) and $E_c^{\text{defect}}(0)/E_c^{1144}(0) = 0.6$ were chosen (for the results using other parameters, see Supplementary information). In this case, ΔE_c shows a weak T dependence below T_c^{defect} owing to the increase of E_c^{defect} . As a result, f_p increases with increasing T , showing a peak around 20 K, which qualitatively agrees with the present observations (Figure 2d). Note that the peak position in $f_p - T$ depends on T_c^{defect} (see Supplementary information), hence T_c^{defect} is likely correlated with T_p in the $H - T$ phase diagram (Figure 4). In addition, the vortex lattice softens with increasing T which allows for a better accommodation of the lattice to the defect structure and hence triggers an order-disorder transition of the vortex lattice. This tendency is compatible with the appearance of second magnetization peak at higher temperatures in CaK1144. Thus, the unusual T dependence of J_c in CaK1144 can be qualitatively understood by considering the SC defects unique to this material. In the present case, the feature is pronounced possibly because (i) CaK1144 is essentially a clean system as indicated by the relatively low J_c at low T and (ii) Ca122 intergrowths take discrete T_c^{defect} values determined by the number of Ca layers, resulting in a single peak in T dependence of J_c . However, to quantify the influence of the Ca122 intergrowths on the unusual T dependence of J_c , further experimental investigations such as determination of defect density as well as more detailed theoretical calculations are desired.

To summarize, we demonstrated a clear correlation between the microstructure and the vortex pinning properties of CaK1144. The nanoscale Ca122 intergrowths inherent to CaK1144 single crystals result in an unusual T dependence of $J_c^{H//c}$ as well as extremely large $J_c^{H//ab}$, distinct from other IBSs. The advantageous vortex pinning properties will offer a new route for further improvement of J_c and enhance the application potentiality of IBSs.

METHODS

Single crystal growth

Single crystals of CaK1144 were grown by the FeAs-flux method.³⁹ The FeAs precursor was prepared from Fe and As mixed at a ratio of 1 : 1 and heated at 900 °C for 10 h in an evacuated quartz tube. Ca, K, and FeAs were weighed at a ratio of 1 : 1.1 : 10 and placed in a zirconia crucible, then sealed in a Ta container using an arc-welding chamber. The Ta container was sealed in an evacuated quartz tube to protect Ta from oxidation. The container was heated during 5 h to 650 °C and held there for 5 h. It was then heated to 1180 °C within 5 h and held there for another 5 h. Then, it was cooled over 5 h to 1050 °C, followed by slow cooling to 930 °C for 80 h. For the single crystals used in this study, X-ray diffraction (XRD) patterns were measured at room temperature using a diffractometer with Cu K α radiation (Rigaku, Ultima IV) to check 00 l peaks (see Supplementary information). No trace of Ca122 and K122 was observed within the resolution of XRD.

Scanning transmission electron microscopy

The microstructure of a CaK1144 single crystal was investigated using an aberration-corrected scanning transmission electron microscope (FEI, Titan cubed) at an acceleration voltage of 300 kV. The sample was prepared using a focused ion beam (Hitachi, FB-2000). The chemical composition was investigated by electron energy loss spectroscopy (EELS, Gatan, GIF Quantum ERS) and energy dispersive X-ray spectroscopy (EDS, Oxford Instruments, X-Max^N 100TLE).

In-plane resistivity measurements

The in-plane resistivity $\rho_{ab}(T)$ (shown in the Supplementary information) was measured by a standard four-probe method using a physical property measurement system (Quantum Design). Magnetic fields up to 9 T were applied along the c axis and in the ab plane to evaluate the anisotropy of upper critical fields. As shown in the Supplementary information, the residual resistivity ratio ($\rho_{ab}(300\text{K})/\rho_{ab}(40\text{K})$) was ~ 16 , and no trace of magneto-structural phase transition of Ca122 phase was observed around 170 K. These properties meet the criteria for “phase-pure” single crystals in Ref. 39.

Magnetization measurements

The samples for the magnetization measurements were cut into rectangular shapes. For CaK1144, the dimensions were $l = 1.57$ mm (length), $w = 1.34$ mm (width), and $d = 0.035$ mm (thickness). For BaK122, the dimensions were $l = 1.59$ mm, $w = 0.764$ mm, and $d = 0.099$ mm. The measurements were performed using a magnetic property measurement system (Quantum Design). For $H // c$, $J_c^{H//c}$ was calculated using Bean’s critical state model⁴⁰; $J_c^{H//c} = 20\Delta M/w(1-w/3l)$ where ΔM is the width of the MHLs. For $H // ab$, two J_c components (in-plane J_c ($J_c^{H//ab}$) and inter-plane J_c (J_c^c)) contribute to M . Here, we used a simplified formula for the evaluation of $J_c^{H//ab}$ by taking $J_c^{H//ab} = J_c^c$, i.e. $J_c^{H//ab} = 20\Delta M/d(1-d/3l)$, following the previous study.³⁰ We confirmed that this simplified procedure does not alter the main conclusions in this study. For more details, see the Supplementary information where the evaluation of $J_c^{H//ab}$ and J_c^c using the extended Bean’s critical state model for anisotropic J_c ^{41,42} is described.

ACKNOWLEDGEMENTS

We thank T. Tamegai and S. Pyon for fruitful discussion on the evaluation of anisotropic J_c . This work was supported by the Austria-Japan Bilateral Joint Research Project hosted by the Japan Society for the Promotion of Science (JSPS) and by FWF: I2814-N36, and a Grant-in-Aid for Scientific Research (KAKENHI) (JSPS Grant Nos. JP16K17510 and JP16H06439).

AUTHOR CONTRIBUTIONS

The research plan was designed and coordinated by A.I., S.I., K.Kawashima, and H.E. S.I., A.I., H.O., N.T., H.A., and M.I. carried out the single crystal growth and the basic characterization of CaK1144 and BaK122. S.I. conducted the electrical transport and the magnetization measurements on the single crystals. K.Y., Y.K., and K.Kimoto performed the STEM measurements and conducted the data analysis. S.I. and M.E. carried out the numerical calculation. S.I. wrote the main body of the manuscript under the support of other coauthors, particularly by M.E., J.S., and H.E.; all authors contributed to the discussion of the results for the manuscript.

References

1. Blatter, G., Feigel'man, M. V., Geshkenbein, V. B., Larkin, A. I. & Vinokur, V. M. Vortices in high-temperature superconductors. *Rev. Mod. Phys.* **66**, 1125–1388 (1994).
2. Foltyn, S. R. *et al.* Materials science challenges for high-temperature superconducting wire. *Nat. Mater.* **6**, 631–642 (2007).
3. Matsumoto, K. & Mele, P. Artificial pinning center technology to enhance vortex pinning in YBCO coated conductors. *Supercond. Sci. Technol.* **23**, 014001 (2010).
4. Obradors, X. & Puig, T. Coated conductors for power applications: materials challenges. *Supercond. Sci. Technol.* **27**, 044003 (2014).
5. Feighan, J. P. F., Kursumovic, A. & MacManus-Driscoll, J. L. Materials design for artificial pinning centres in superconductor PLD coated conductors. *Supercond. Sci. Technol.* **30**, 123001 (2017).
6. Haugan, T., Barnes, P. N., Wheeler, R., Meisenkothen, F. & Sumption, M. Addition of nanoparticle dispersions to enhance flux pinning of the $\text{YBa}_2\text{Cu}_3\text{O}_{7-x}$ superconductor. *Nature* **430**, 867–870 (2004).
7. MacManus-Driscoll, J. L. *et al.* Strongly enhanced current densities in superconducting coated conductors of $\text{YBa}_2\text{Cu}_3\text{O}_{7-x} + \text{BaZrO}_3$. *Nat. Mater.* **3**, 439–443 (2004).
8. Gutiérrez, J. *et al.* Strong isotropic flux pinning in solution-derived $\text{YBa}_2\text{Cu}_3\text{O}_{7-x}$ nanocomposite superconductor films. *Nat. Mater.* **6**, 367–373 (2007).
9. Llordés, A. *et al.* Nanoscale strain-induced pair suppression as a vortex-pinning mechanism in high-temperature superconductors. *Nat. Mater.* **11**, 329–336 (2012).
10. van Dover, R. B. *et al.* Critical currents near 10^6 A cm^{-2} at 77 K in neutron-irradiated single-crystal $\text{YBa}_2\text{Cu}_3\text{O}_7$. *Nature* **342**, 55–57 (1989).
11. Civale, L. *et al.* Vortex confinement by columnar defects in $\text{YBa}_2\text{Cu}_3\text{O}_7$ crystals: Enhanced pinning at high fields and temperatures. *Phys. Rev. Lett.* **67**, 648–651 (1991).
12. Leroux, M. *et al.* Rapid doubling of the critical current of $\text{YBa}_2\text{Cu}_3\text{O}_{7-\delta}$ coated conductors for viable high-speed

- industrial processing. *Appl. Phys. Lett.* **107**, 192601 (2015).
13. Hosono, H., Yamamoto, A., Hiramatsu, H. & Ma, Y. Recent advances in iron-based superconductors toward applications. *Mater. Today* **21**, 278–302 (2018).
 14. Sakoda, M., Iida, K. & Naito, M. Recent progress in thin-film growth of Fe-based superconductors: superior superconductivity achieved by thin films. *Supercond. Sci. Technol.* **31**, 093001 (2018).
 15. Eisterer, M. Radiation effects on iron-based superconductors. *Supercond. Sci. Technol.* **31**, 013001 (2018).
 16. Miura, M. *et al.* Strongly enhanced flux pinning in one-step deposition of BaFe₂(As_{0.66}P_{0.33})₂ superconductor films with uniformly dispersed BaZrO₃ nanoparticles. *Nat. Commun.* **4**, 2499 (2013).
 17. Lee, J. *et al.* High critical current density over 1 MA cm⁻² at 13 T in BaZrO₃ incorporated Ba(Fe,Co)₂As₂ thin film. *Supercond. Sci. Technol.* **30**, 085006 (2017).
 18. Lee, S. *et al.* Artificially engineered superlattices of pnictide superconductors. *Nat. Mater.* **12**, 392–396 (2013).
 19. Hänisch, J. *et al.* High field superconducting properties of Ba(Fe_{1-x}Co_x)₂As₂ thin films. *Sci. Rep.* **5**, 17363 (2015).
 20. Yuan, P., Xu, Z., Wang, D. & Zhang, M. Vortex pinning properties in Co-doped BaFe₂As₂ thin films with a high critical current density over 2 MA cm⁻² at 9T. *Supercond. Sci. Technol.* **30**, 025001 (2017).
 21. Shimoyama, J. Potentials of iron-based superconductors for practical future materials. *Supercond. Sci. Technol.* **27**, 044002 (2014).
 22. Pallecchi, I., Eisterer, M., Malagoli, A. & Putti, M. Application potential of Fe-based superconductors. *Supercond. Sci. Technol.* **28**, 114005 (2015).
 23. Hosono, H. & Kuroki, K. Iron-based superconductors: Current status of materials and pairing mechanism. *Phys. C* **514**, 399–422 (2015).
 24. Song, D. *et al.* Distinct doping dependence of critical temperature and critical current density in Ba_{1-x}K_xFe₂As₂ superconductor. *Sci. Rep.* **6**, 26671 (2016).
 25. Prozorov, R. *et al.* Intrinsic pinning on structural domains in underdoped single crystals of Ba(Fe_{1-x}Co_x)₂As₂. *Phys. Rev. B* **80**, 174517 (2009).
 26. Demirdiř, S. *et al.* Disorder, critical currents, and vortex pinning energies in isovalently substituted BaFe₂(As_{1-x}P_x)₂. *Phys. Rev. B* **87**, 094506 (2013).
 27. Ishida, S. *et al.* Doping-dependent critical current properties in K, Co, and P-doped BaFe₂As₂ single crystals. *Phys. Rev. B* **95**, 014517 (2017).
 28. Iyo, A. *et al.* New-Structure-Type Fe-Based Superconductors: CaAF₄As₄ (A = K, Rb, Cs) and SrAF₄As₄ (A = Rb, Cs). *J. Am. Chem. Soc.* **138**, 3410–3415 (2016).
 29. Kawashima, K. *et al.* Superconductivity in Fe-Based Compound EuAF₄As₄ (A = Rb and Cs). *J. Phys. Soc. Japan* **85**, 064710 (2016).
 30. Singh, S. J. *et al.* Ultrahigh critical current densities, the vortex phase diagram, and the effect of granularity of the stoichiometric high-T_c superconductor CaKFe₄As₄. *Phys. Rev. Mater.* **2**, 074802 (2018).
 31. Cheng, W., Lin, H., Shen, B. & Wen, H. H. Comparative study of vortex dynamics in CaKFe₄As₄ and Ba_{0.6}K_{0.4}Fe₂As₂ single crystals. *Sci. Bull.* **64**, 31–39 (2019).
 32. van der Beek, C. J. *et al.* Quasiparticle Scattering Induced by Charge Doping of Iron-Pnictide Superconductors Probed by Collective Vortex Pinning. *Phys. Rev. Lett.* **105**, 267002 (2010).

33. Tarantini, C. *et al.* Intrinsic and extrinsic pinning in NdFeAs(O,F): Vortex trapping and lock-in by the layered structure. *Sci. Rep.* **6**, 36047 (2016).
34. Altarawneh, M. M. *et al.* Determination of anisotropic H_{c2} up to 60 T in $\text{Ba}_{0.55}\text{K}_{0.45}\text{Fe}_2\text{As}_2$ single crystals. *Phys. Rev. B* **78**, 220505 (2008).
35. Yuan, H. Q. *et al.* Nearly isotropic superconductivity in $(\text{Ba,K})\text{Fe}_2\text{As}_2$. *Nature* **457**, 565–568 (2009).
36. Meier, W. R. *et al.* Anisotropic thermodynamic and transport properties of single-crystalline $\text{CaKFe}_4\text{As}_4$. *Phys. Rev. B* **94**, 064501 (2016).
37. Tamegai, T. *et al.* Effects of particle irradiations on vortex states in iron-based superconductors. *Supercond. Sci. Technol.* **25**, 084008 (2012).
38. Mikitik, G. P. & Brandt, E. H. Critical state in thin anisotropic superconductors of arbitrary shape. *Phys. Rev. B* **62**, 6800–6811 (2000).
39. Meier, W. R., Kong, T., Bud'ko, S. L. & Canfield, P. C. Optimization of the crystal growth of the superconductor $\text{CaKFe}_4\text{As}_4$ from solution in the FeAs – CaFe_2As_2 – KFe_2As_2 system. *Phys. Rev. Mater.* **1**, 013401 (2017).
40. Bean, C. P. Magnetization of high-field superconductors. *Rev. Mod. Phys.* **36**, 31–39 (1964).
41. Gyorgy, E. M., van Dover, R. B., Jackson, K. A., Schneemeyer, L. F. & Waszczak, J. V. Anisotropic critical currents in $\text{Ba}_2\text{YCu}_3\text{O}_7$ analyzed using an extended Bean model. *Appl. Phys. Lett.* **55**, 283 (1989).
42. Pyon, S. *et al.* Large and significantly anisotropic critical current density induced by planar defects in $\text{CaKFe}_4\text{As}_4$ single crystals. *Phys. Rev. B* **99**, 104506 (2019).

FIGURES

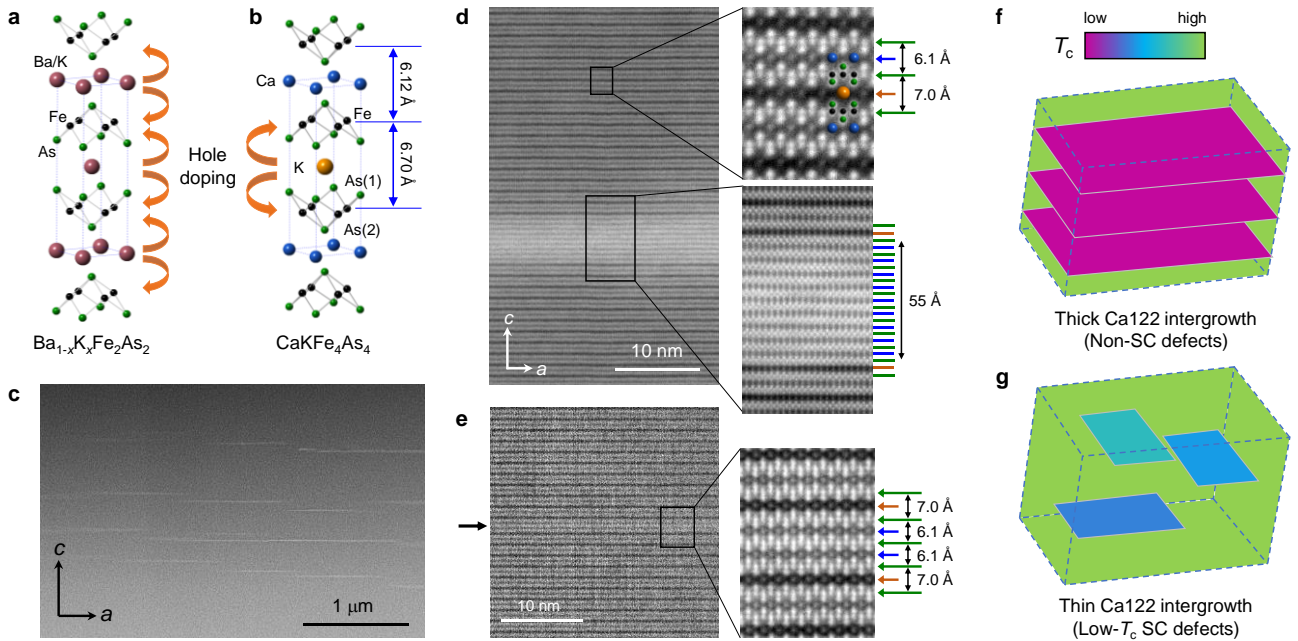


Fig. 1 Microstructure of CaK1144 single crystal investigated by STEM. **a,b** Crystal structure of BaK122 and CaK1144. **c** STEM image with low magnification. A number of defects (bright lines) with length of $\sim 1 \mu\text{m}$ can be identified. **d** High resolution STEM image around the defects shown in **c**. A magnified view of the CaK1144 matrix and the defect are shown in right upper and lower panels, respectively. The structural model of CaK1144 is overlapped in the upper panel in accordance with the observed STEM image. The defect with thickness of 55 \AA (each Fe-Fe interplane distance is 6.1 \AA) is found to be Ca122 intergrowth. We did not observe intergrowths of KFe_2As_2 nor FeAs (flux material) inclusions. **e** Thin defect observed by STEM and the enlarged view, demonstrating a monolayer Ca122 intergrowth. **f,g** Schematic models for thick and thin Ca122 intergrowths. Colour gradation indicates T_c . Thick intergrowths are regarded as non-superconducting planar defects, while thin ones are considered to be superconducting defects with a lower T_c than in the CaK1144 matrix. Such intergrowths act as effective pinning centres, giving rise to the unusual J_c properties in CaK1144.

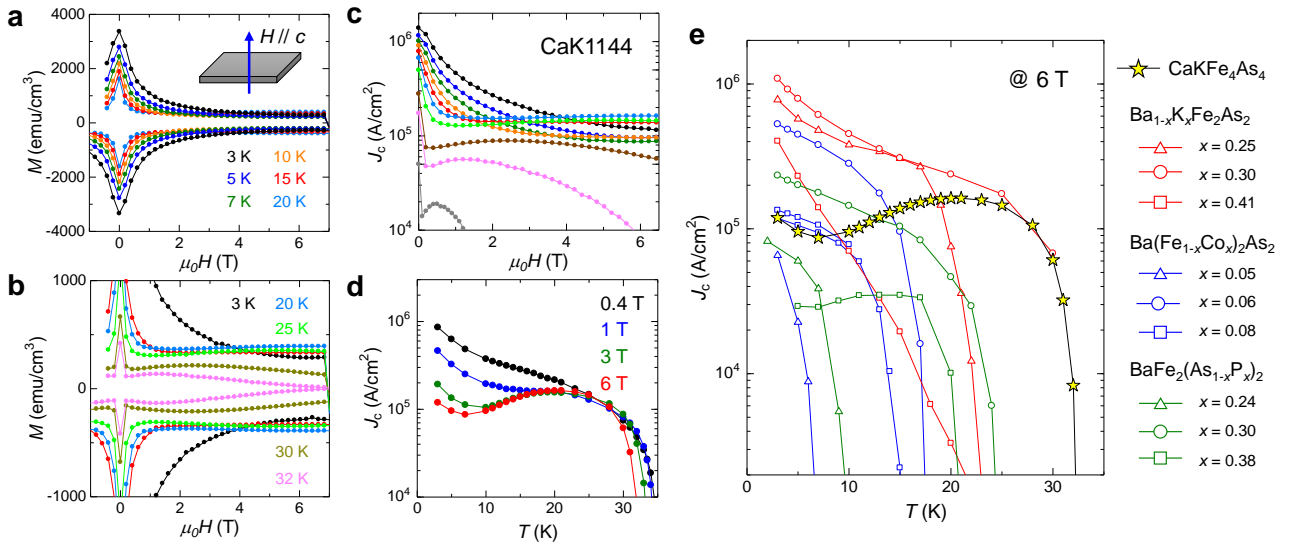


Fig. 2 Critical current properties of CaK1144 single crystal for $H // c$. **a** MHLs at $T = 3$ – 20 K. **b** MHLs at $T = 3$ K and 20 – 32 K. **c** Magnetic field dependence of J_c . **d** Temperature dependence of J_c at $\mu_0 H = 0.4, 1, 3,$ and 6 T. **e** Comparison of J_c with representative 122 single crystals²⁷, BaK122 (red), Co-Ba122 (blue), and P-Ba122 (green) with various doping concentrations x . In addition to CaK1144, P-Ba122 with $x = 0.38$ shows an increase in J_c with increasing T . In this case, however, a MHL is characterized by a sharp second magnetization peak, which is apparently different from CaK1144²⁷.

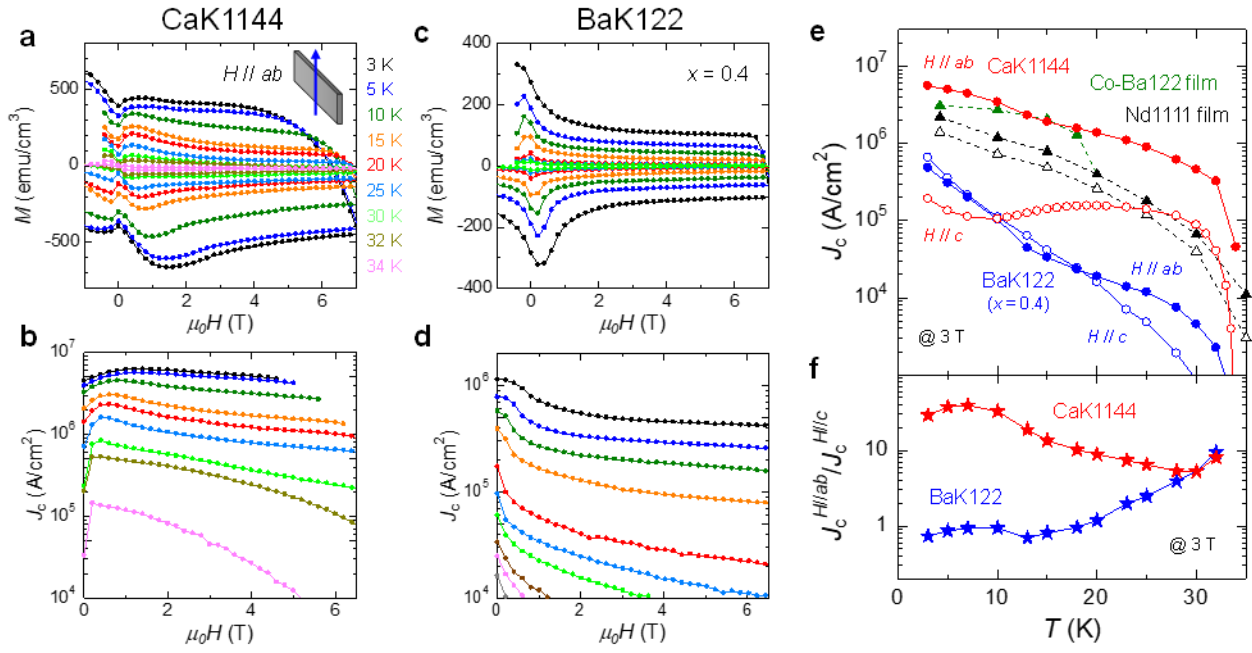


Fig. 3 Critical current properties of CaK1144 single crystal for $H // ab$ in comparison with BaK122 ($x = 0.4$). **a,b** MHLs at $T = 3\text{--}34$ K and magnetic field dependence of J_c for CaK1144. **c,d** Same data set as in **a, b** for BaK122. **e** Temperature dependence of J_c for CaK1144 (red) and BaK122 (blue) under $H // ab$ (filled) and c (open). J_c data of Co-Ba122²⁰ and Nd1111³³ thin films are plotted for comparison. Note that J_c of Co-Ba122 film is almost isotropic. **f** Temperature dependence of J_c anisotropy defined as $J_c^{H//ab}/J_c^{H//c}$.

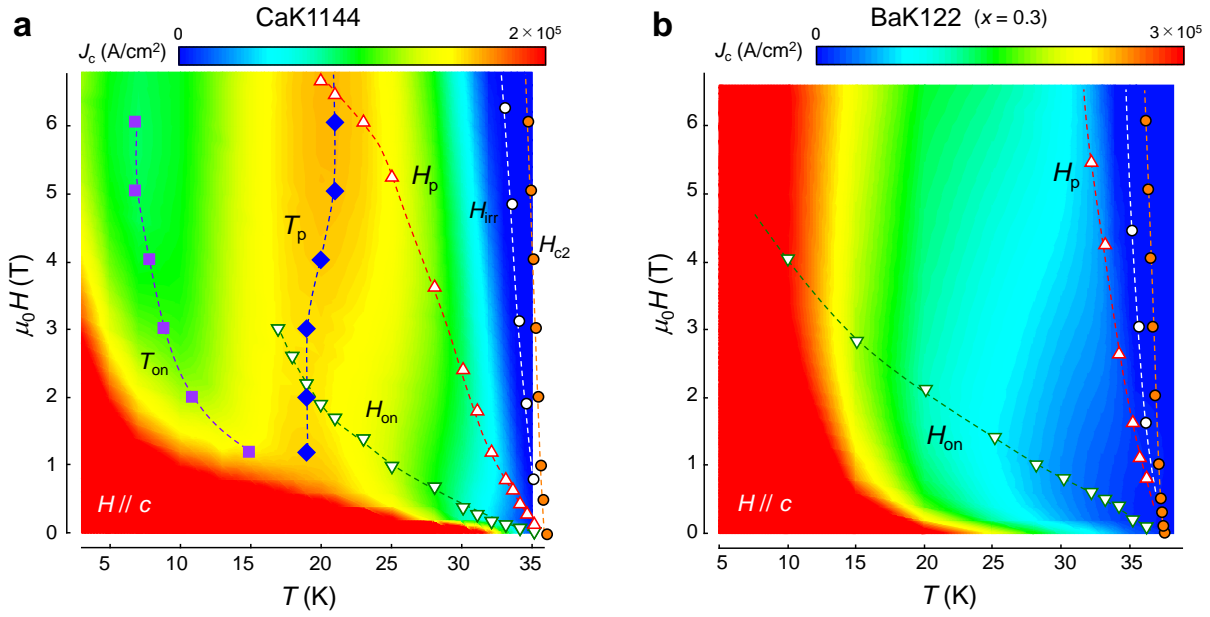


Fig. 4 Vortex phase diagrams under $H // c$ for **a** CaK1144 and **b** BaK122 ($x = 0.3$). H and T dependences of J_c are shown in the form of contour plots. Hot (cold) colours indicate high (low) J_c region. Several characteristic T and H are plotted: T_{on} , the onset of the peak effect in $J_c - T$ curves defined by the local minimum (purple squares); T_p , the peak position in $J_c - T$ (blue diamonds); H_{on} , the onset of the second magnetization peak in $M - H$ curves defined by the local minimum (open reversed triangles); H_p , the second peak position in $M - H$ (open triangles); H_{irr} , irreversibility field defined by a criterion of $J_c < 100$ A/cm² (open circles); and H_{c2} , the upper critical field along the c axis obtained from the resistivity measurements (orange circles). The dashed lines are guide for the eye.

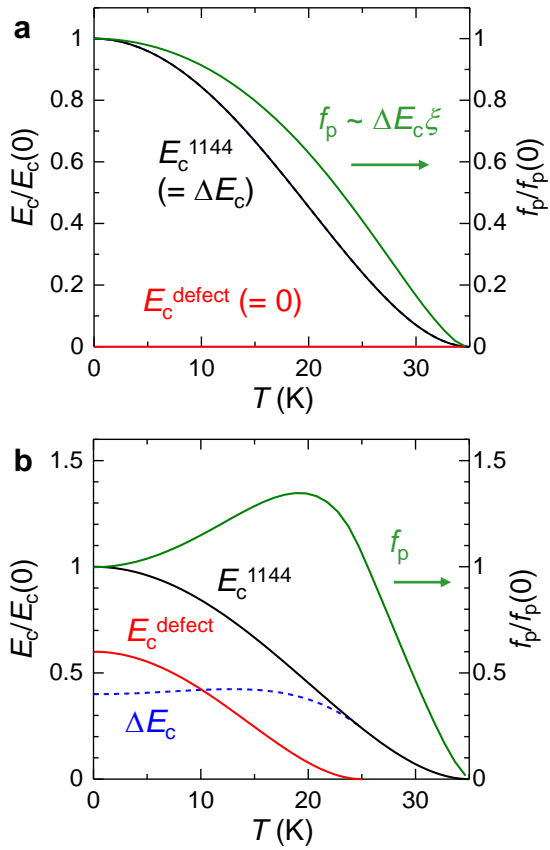


Fig. 5 Temperature dependence of pinning force density f_p . **a** f_p ($\sim \Delta E_c \xi$, green curve) calculated for non-SC defects where $E_c^{\text{defect}} = 0$ (red curve), i.e. $\Delta E_c = E_c^{1144}$ (black curve). In this case, f_p monotonically decreases with increasing T . **b** f_p calculated for SC defects with $T_c^{\text{defect}} = 25$ K and $E_c^{\text{defect}}(0)/E_c^{1144}(0) = 0.6$. ΔE_c (blue dashed curve) shows a weak T dependence below T_c^{defect} , resulting in an enhancement of f_p with increasing T .

Supplementary Information for

Unique defect structure and advantageous vortex pinning properties in superconducting $\text{CaKFe}_4\text{As}_4$

Shigeyuki Ishida^{1*}, Akira Iyo¹, Hiraku Ogino¹, Hiroshi Eisaki¹, Nao Takeshita¹, Kenji Kawashima², Keiichi Yanagisawa³, Yuuga Kobayashi³, Koji Kimoto³, Hideki Abe³, Motoharu Imai³, Jun-ichi Shimoyama⁴, and Michael Eisterer⁵

¹Electronic and Photonics Research Institute, National Institute of Advanced Industrial Science and Technology (AIST), Tsukuba, Ibaraki 305-8568, Japan

²IMRA Materials R&D Co., Ltd., Kariya, Aichi 448-0032, Japan

³National Institute for Materials Science (NIMS), Tsukuba, Ibaraki 305-0047, Japan

⁴Department of Physics and Mathematics, Aoyama Gakuin University, Sagamihara, Kanagawa 252-5258, Japan

⁵Atominstytut, TU Wien, Stadionallee 2, 1020 Vienna, Austria

*corresponding author: s.ishida@aist.go.jp

1. Characterization of $\text{CaKFe}_4\text{As}_4$ and $\text{Ba}_{0.6}\text{K}_{0.4}\text{Fe}_2\text{As}_2$ single crystals

In advance of the scanning transmission electron microscopy (STEM) and magnetization hysteresis loop (MHL) measurements, the quality of $\text{CaKFe}_4\text{As}_4$ (CaK1144) single crystals was checked by X-ray diffraction (XRD), magnetization (M) and in-plane resistivity (ρ_{ab}) measurements following the procedure in Ref. 1.

X-ray diffraction measurement

Figure S1 shows a XRD pattern of a CaK1144 sample presented on a log scale. All the peaks can be indexed by $00l$ for CaK1144. The small peaks indicated by blue triangles arise from the residual Cu $K\beta$ radiation. No trace of CaFe_2As_2 (Ca122) and KFe_2As_2 (K122) phases was observed within the resolution of in-lab XRD.

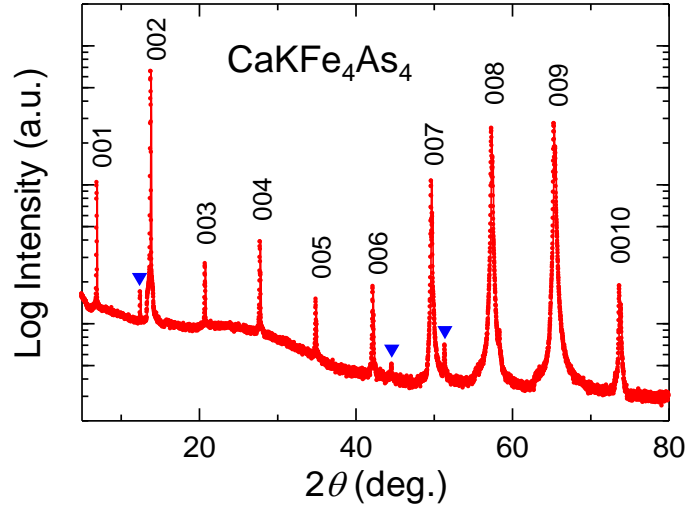


Fig. S1 XRD patterns for a CaK1144 single crystal. Blue triangles indicate residual Cu $K\beta$ reflections.

Magnetization and in-plane resistivity

Next, Figure S2a shows temperature (T) dependence of M of CaK1144. M was measured with zero-field-cooled and field-cooled processes under a magnetic field (H) of 1 mT along the c axis. A sharp superconducting transition was observed around onset $T_c = 35.5$ K. There is no trace of additional transition around $T = 3.8$ K arising from K122. Figure S2b shows T dependence of ρ_{ab} . ρ_{ab} shows a metallic behavior characterized by a S-shaped curve, which is similar to that observed for optimally-doped BaK122 (see Figure S2f). No anomaly corresponding to magneto-structural transition of Ca122 was detected in ρ_{ab} . The residual resistivity ratio $\rho_{ab}(300\text{K})/\rho_{ab}(40\text{K})$ is about 16, which is comparable with that for the best sample shown in Ref. 1. Thus, the results of XRD, M , and ρ_{ab} measurements suggest that a “phase-pure” CaK1144 single crystal was obtained. We performed STEM experiments on such a selected crystal.

We also evaluated the anisotropy of upper critical field (H_{c2}). Figure S2c shows ρ_{ab} of CaK1144 under H along c axis (upper panel) and ab plane (lower panel) measured up to $\mu_0 H = 9$ T. The superconducting transition shifts toward lower temperatures with increasing H . The broadening of the transition is weak, which can be associated with the small anisotropy of CaK1144. Figure S2d shows the T dependence of H_{c2} for $H \parallel c$ (blue) and ab (green) obtained from 90% (filled) and 10% (open) criteria shown in Figure S2c. The slope (dH_{c2}/dT) was estimated

by a linear fit to 1-9 T data, and $|dH_{c2}/dT| \sim 5.5$ T/K and ~ 9.9 T/K were obtained for $H // c$ and ab , respectively. Using the Werthamer-Helfand-Hohenberg formula ($H_{c2}(0) = 0.69T_c|dH_{c2}/dT|$), $H_{c2}(0)$ was estimated to be 140 T and 240 T for $H // c$ and ab , respectively. The anisotropy factor (γ) is about 1.8. These superconducting properties are comparable with those for BaK122 (for comparison, the same data set as in Figures S2a-d is shown in Figures S2e-h).

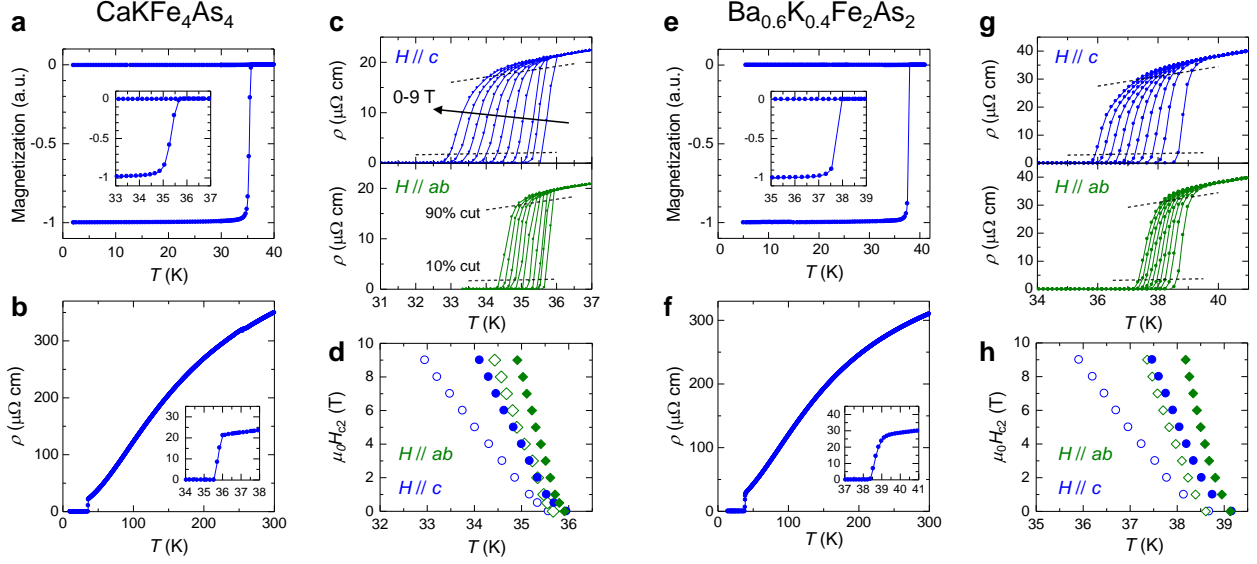


Fig. S2 Characterization of CaK1144 and BaK122 single crystals. **a** T dependence of M for CaK1144. Inset shows the magnified view around the superconducting transition. **b** T dependence of ρ_{ab} . Inset shows the magnified view around the superconducting transition. **c** ρ_{ab} under the magnetic fields up to 9 T for $H // c$ (upper panel) and ab (lower panel). **d** T dependence of H_{c2} for $H // c$ (blue) and ab (green). Filled and open symbols indicate H_{c2} determined by 90% and 10% criteria (shown in Figure S2c), respectively. **e-f** The same data set as shown in **a-d** for BaK122.

2. Chemical composition analysis of CaK1144

The chemical compositions of CaK1144 and defects were investigated by electron energy loss spectroscopy (EELS) and energy dispersive X-ray spectroscopy (EDS). Figure S3a shows the ADF-STEM image and EELS spectra around a defect in CaK1144 matrix (indicated by a black arrow). The alternation of Ca and K layers is violated; two Ca layers appears (or a K layer is skipped) around the defect. Meanwhile, no significant change was found for Fe and As. Similar results were obtained by EDS as shown in Figure S3b. In addition, the average chemical composition away from the defect is Ca : K : Fe : As = 11.0 : 10.7 : 41.2 : 37.1, which agrees with CaK1144 within the measurement error range of EDS.

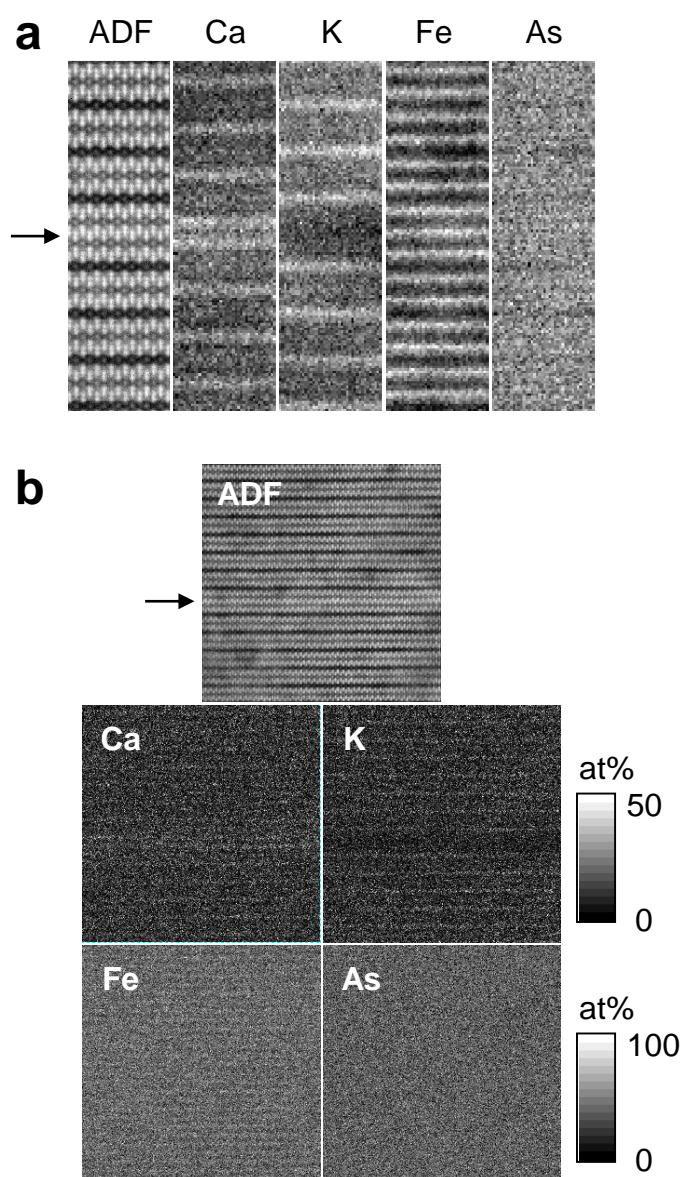


Fig. S3 Chemical composition analysis of CaK1144. **a** ADF-STEM image and EELS spectra, and **b** ADF-STEM image and EDS mapping around a defect (indicated by black arrows) in CaK1144 matrix.

3. Temperature dependence of J_c for $H \parallel c$

Figure S4a shows the T dependence of J_c for $H \parallel c$ ($J_c^{H \parallel c} - T$) under 1, 1.4, and 2 T. The peak in $J_c^{H \parallel c} - T$ (T_p) can be defined for $H > 1$ T, while it is absent at low H below 1 T (a shoulder feature remains). This behavior can be understood by taking into account the two source of vortex pinning; the strong vortex pinning and the superconducting (SC) defects. Figure S4b shows the $J_c^{H \parallel c} - T$ curves plotted in the double logarithmic scale. At low T and H , $J_c^{H \parallel c}$ shows a power-law decay ($J_c \sim H^{-0.7}$), which is observed in various iron-based superconductors and often associated with the strong vortex pinning arising from the sparse and large pointlike defects.² At low H , the strong pinning contribution, which monotonically decreases with T , is likely dominant, resulting in the monotonous decrease of J_c . On the other hand, since the strong pinning contribution rapidly decreases in H , the pinning arising from the SC defects (thin Ca122 intergrowths) which is enhanced with increasing T becomes dominant at higher H , thus T_p can be clearly observed.

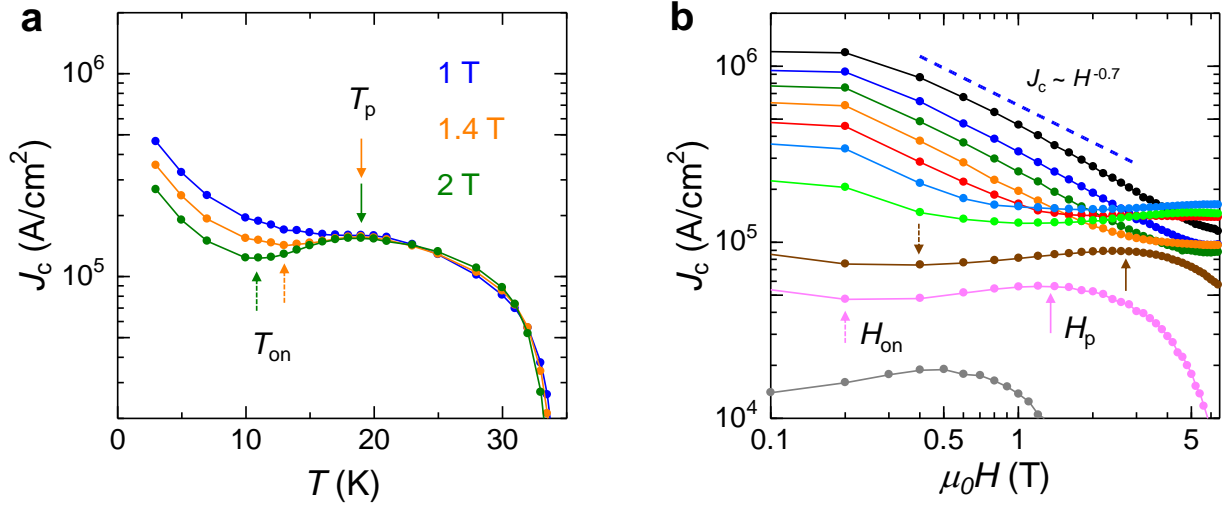


Fig. S4 T and H dependence of $J_c^{H \parallel c}$. **a** T dependence of $J_c^{H \parallel c}$ under 1, 1.4, and 2 T. The peak (T_p) and local minimum (T_{on}) are indicated by solid and dashed arrows, respectively. **b** H dependence of $J_c^{H \parallel c}$ plotted in the double logarithmic scale. The dashed line shows a power-law relation, $J_c \sim H^{-0.7}$. The peak (H_p) and local minimum (H_{on}) are indicated by solid and dashed arrows, respectively.

4. Calculation of pinning force density

The pinning force density (f_p) was calculated using a simple model. For pinning centres larger than coherence length (ξ), the pinning energy (E_p) is proportional to $\Delta E_c \xi^2$ where ΔE_c is the difference in condensation energy between SC defect and Ca1144 matrix, hence we obtain $f_p \sim E_p/\xi \sim \Delta E_c \xi$. Here, the T dependences of E_c and ξ are modelled by $E_c \sim H_c^2 \sim [1 - (T/T_c)^2]^2$ (H_c : thermodynamic critical field) and $\xi \sim [(1 + (T/T_c)^2)/(1 - (T/T_c)^2)]^{1/2}$, respectively. In Figure S5, the calculation results using different T_c^{defect} and $E_c^{\text{defect}}(0)/E_c^{1144}(0)$ values are shown. It can be seen that the peak position of f_p shifts to lower T when T_c^{defect} is lowered and that the peak is more prominent when $E_c^{\text{defect}}(0)/E_c^{1144}(0)$ is closer to 1. This simple model suggests that T_c^{defect} is correlated with T_p in $J_c^{H//c} - T$ curves.

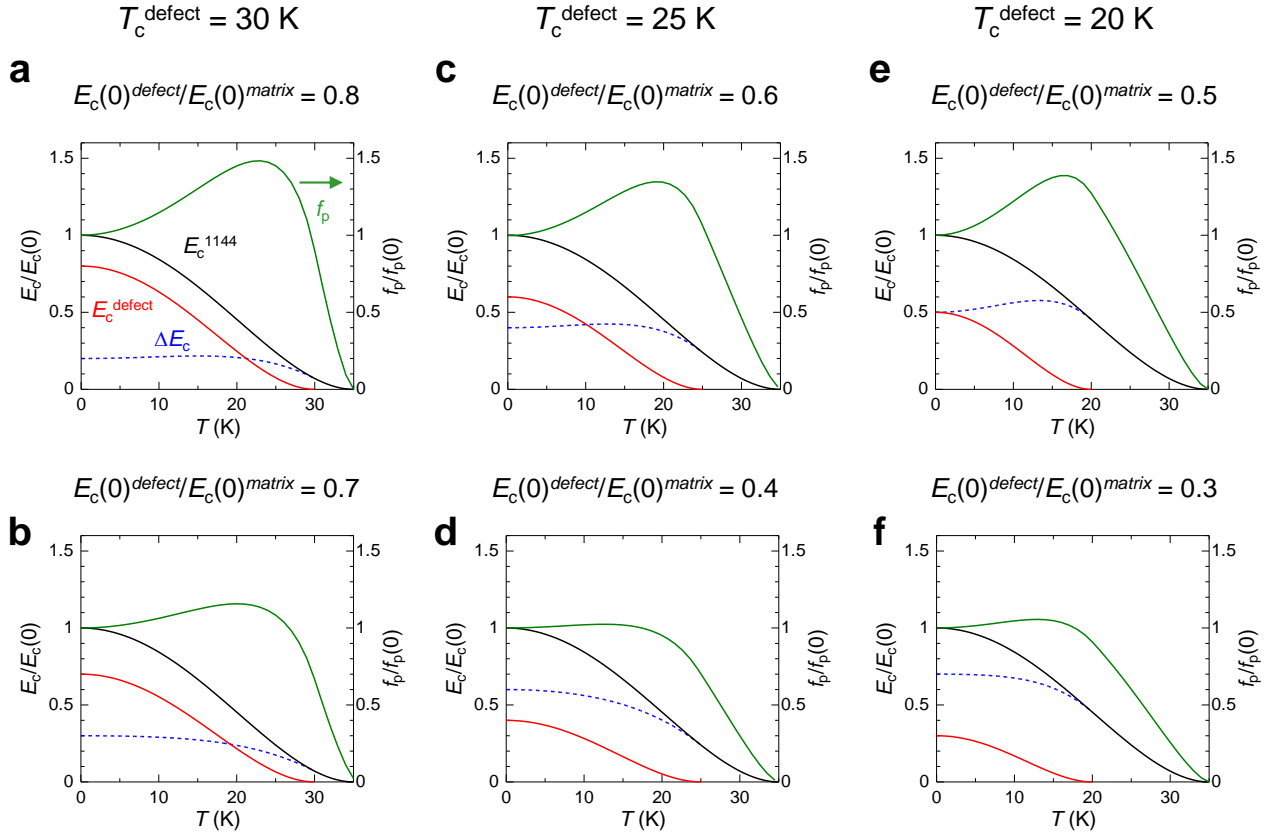


Fig. S5 Temperature dependence of pinning force density f_p . **a,b** f_p calculated using $T_c^{\text{defect}} = 30$ K and $E_c^{\text{defect}}(0)/E_c^{1144}(0) = 0.8$ and 0.7 , **c,d** $T_c^{\text{defect}} = 25$ K and $E_c^{\text{defect}}(0)/E_c^{1144}(0) = 0.6$ and 0.4 , and **e,f** $T_c^{\text{defect}} = 20$ K and $E_c^{\text{defect}}(0)/E_c^{1144}(0) = 0.5$ and 0.3 , respectively.

5. Calculation of anisotropic J_c for $H \parallel ab$

In the manuscript, we evaluated $J_c^{H//ab}$ using a simplified formula by taking $J_c^{H//ab} = J_c^c$. Meanwhile, to evaluate $J_c^{H//ab}$ more properly, two J_c components, i.e. $J_c^{H//ab}$ and J_c^c should be considered. Here, we describe the calculation procedure of $J_c^{H//ab}$ and J_c^c based on the extended Bean's critical state model for anisotropic J_c .^{3,4}

First, because there are two J_c components, we need to perform two independent $M - H$ measurements on a rectangular sample with dimensions of l , w ($< l$), and d ($\parallel c$) using different setups as shown in Figure S6.

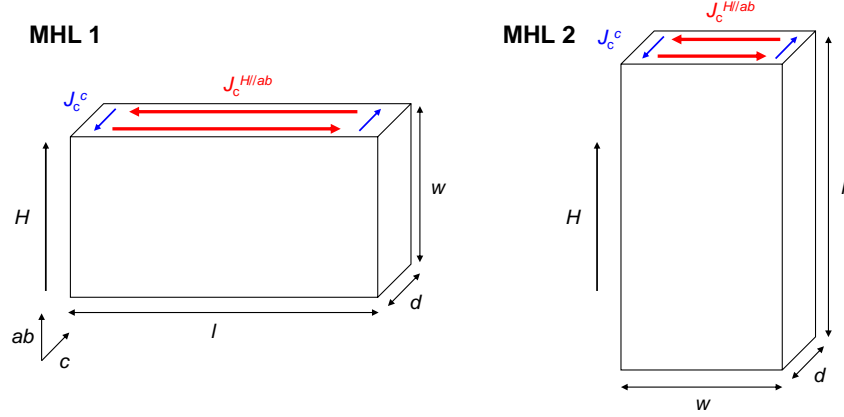


Fig. S6 Two independent $M - H$ measurement setups for the evaluation of anisotropic J_c , $J_c^{H//ab}$ and J_c^c , using extended Bean's critical state model. H is applied along w (MHL 1) and l (MHL 2).

Next, as described in the reference paper,³ different current-flow configurations should be adopted for the calculation depending on the relation between the sample shape (l/d or w/d) and the magnitude of J_c anisotropy ($J_c^{H//ab}/J_c^c$). The possible configurations are shown in Figure S7 together with the conditions of $J_c^{H//ab}/J_c^c$ for each pattern.

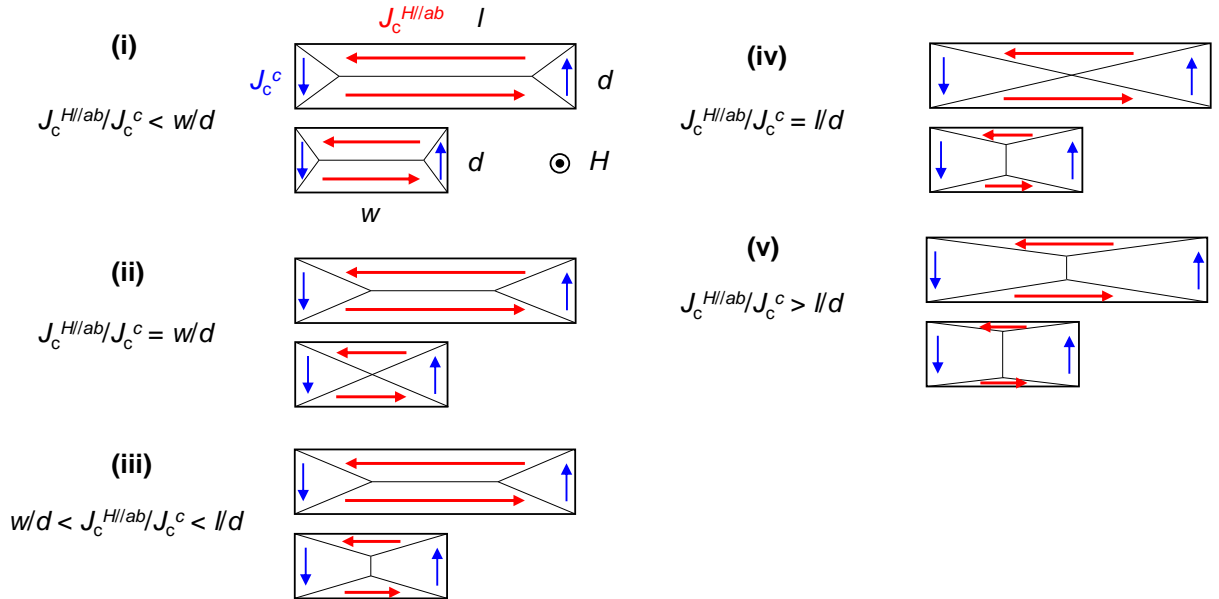


Fig. S7 Possible configurations of the current flows for $H \parallel ab$. The conditions of $J_c^{H//ab}/J_c^c$ for each configuration are also shown.

Based on these configurations, the width of MHL, ΔM_1 and ΔM_2 for MHL 1 and MHL 2, respectively, can be expressed by the following equations:

$$\Delta M_1 = \begin{cases} \frac{d J_c^{H//ab}}{20} \left(1 - \frac{d J_c^{H//ab}}{3l J_c^c} \right) & \text{(for (i) and (iii))} \\ \frac{l J_c^c}{20} \left(1 - \frac{l J_c^c}{3d J_c^{H//ab}} \right) & \text{(for (v))} \end{cases}$$

$$\Delta M_2 = \begin{cases} \frac{d J_c^{H//ab}}{20} \left(1 - \frac{d J_c^{H//ab}}{3w J_c^c} \right) & \text{(for (i))} \\ \frac{w J_c^c}{20} \left(1 - \frac{w J_c^c}{3d J_c^{H//ab}} \right) & \text{(for (iii) and (v))} \end{cases}$$

Using ΔM_1 and ΔM_2 , $J_c^{H//ab}$ and J_c^c for cases (i), (iii), and (v) in Figure S7 can be calculated as follows (here we define $\alpha = w/l (< 1)$):

$$\text{For (i): } J_c^{H//ab}/J_c^c < w/d \quad J_c^{H//ab} = \frac{20 (\Delta M_1 - \alpha \Delta M_2)}{t (1 - \alpha)}$$

$$J_c^c = \frac{20 (\Delta M_1 - \alpha \Delta M_2)^2}{3w (1 - \alpha)(\Delta M_1 - \Delta M_2)}$$

$$\text{For (iii): } w/d < J_c^{H//ab}/J_c^c < l/d \quad \left[\frac{\alpha d^3}{3} - \frac{\alpha^2 d^3}{27} \right] J_c^{H//ab 3} - 20 \left[\frac{\alpha d^2}{3} \Delta M_1 + d^2 \Delta M_2 \right] J_c^{H//ab 2} + 800d \Delta M_1 \Delta M_2 J_c^{H//ab} - 8000 \Delta M_1^2 \Delta M_2 = 0$$

$$\left[\frac{w^3}{3} - \frac{\alpha w^3}{27} \right] J_c^{c 3} - 20 \left[w^2 \Delta M_1 + \frac{w^2}{3} \Delta M_2 \right] J_c^{c 2} + 800w \Delta M_1 \Delta M_2 J_c^c - 8000 \Delta M_1 \Delta M_2^2 = 0$$

$$\text{For (v): } l/d < J_c^{H//ab}/J_c^c \quad J_c^{H//ab} = \frac{20 (\Delta M_2 - \alpha^2 \Delta M_1)^2}{3\alpha d (1 - \alpha)(\Delta M_2 - \alpha \Delta M_1)}$$

$$J_c^c = \frac{20 (\Delta M_2 - \alpha^2 \Delta M_1)}{w (1 - \alpha)}$$

Then, in order to calculate $J_c^{H//ab}$ and J_c^c from the experimental data, the equations (cases (i), (iii), and (v)) should be appropriately chosen. To determine which equations to use, $\Delta M_1/\Delta M_2$ is a useful parameter which can be easily obtained from the data. From the expressions of ΔM_1 and ΔM_2 shown before, $\Delta M_1/\Delta M_2$ for each case can be described as follows:

$$\frac{\Delta M_1}{\Delta M_2} = \begin{cases} \frac{1 - \frac{d J_c^{H//ab}}{3l J_c^c}}{1 - \frac{d J_c^{H//ab}}{3w J_c^c}} & (J_c^{H//ab}/J_c^c < w/d ; \text{ for (i)}) \\ \frac{d J_c^{H//ab}}{w J_c^c} \frac{1 - \frac{d J_c^{H//ab}}{3l J_c^c}}{1 - \frac{w J_c^c}{3d J_c^{H//ab}}} & (w/d < J_c^{H//ab}/J_c^c < l/d ; \text{ for (iii)}) \\ \frac{l}{w} \frac{1 - \frac{l J_c^c}{3d J_c^{H//ab}}}{1 - \frac{w J_c^c}{3d J_c^{H//ab}}} & (l/d < J_c^{H//ab}/J_c^c ; \text{ for (v)}) \end{cases}$$

For the specific cases, (ii) and (iv), $\Delta M_1/\Delta M_2$ becomes

$$\frac{\Delta M_1}{\Delta M_2} = \begin{cases} \frac{3 - \alpha}{2} & (J_c^{H//ab}/J_c^c = w/d ; \text{ case (ii)}) \\ \frac{2}{\alpha(3 - \alpha)} & (J_c^{H//ab}/J_c^c = l/d ; \text{ case (iv)}) \end{cases}$$

Thus, one can choose cases (i), (iii), and (v) for $\Delta M_1/\Delta M_2 < (3 - \alpha)/2$, $(3 - \alpha)/2 < \Delta M_1/\Delta M_2 < 2/\alpha(3 - \alpha)$, and $2/\alpha(3 - \alpha) < \Delta M_1/\Delta M_2$, respectively.

Below, we show the calculation results for a CaK1144 sample with dimensions of $l = 1.26$ mm, $w = 0.80$ mm, and $d = 0.064$ mm. Figure S8a shows the two MHLs, M_1 and M_2 , obtained from different setups. Clearly, ΔM_1 and ΔM_2 are different from each other ($\Delta M_1 > \Delta M_2$). Here, the values of $(3 - \alpha)/2$ and $2/\alpha(3 - \alpha)$ are 1.18 and 1.33 ($\alpha = w/l = 0.635$), respectively, and $\Delta M_1/\Delta M_2$ takes 1.19-1.26, thus the case (iii) ($(3 - \alpha)/2 < \Delta M_1/\Delta M_2 < 2/\alpha(3 - \alpha)$) was chosen. Figure S8b shows the obtained $J_c^{H//ab}$ (red circles) and J_c^c (blue circles) using the equations for case (iii). The anisotropy of J_c , $J_c^{H//ab}/J_c^c$, is found to be 13-15, confirming a large anisotropy. Thus, we successfully derived $J_c^{H//ab}$ and J_c^c based on the extended Bean's critical state model.

In addition, we calculated $J_c^{H//ab}$ from each single MHL (M_1 or M_2) using the simplified formula by taking $J_c^{H//ab} = J_c^c$. The $J_c^{H//ab}$ values from M_1 and M_2 are shown in Figure S8b (open circles and triangles, respectively). Owing to the averaging of two components, $J_c^{H//ab}$ is underestimated. Meanwhile, it can be seen that $J_c^{H//ab}$ derived from M_1 (open circles) is closer to $J_c^{H//ab}$ from the extended Bean model (red circles) compared with $J_c^{H//ab}$ derived from M_2 (open triangles), indicating that the effect of anisotropy on evaluation of $J_c^{H//ab}$ becomes less significant when $l \gg d$. The data shown in the manuscript were obtained for the sample with $l/d = 45$, which is larger than that of the present sample ($l/d = 20$), hence the contribution from J_c^c should be practically negligible. Thus, we confirmed that $J_c^{H//ab}$ was reasonably evaluated by the simplified calculation and that the procedure does not alter the discussion nor conclusions in this study.

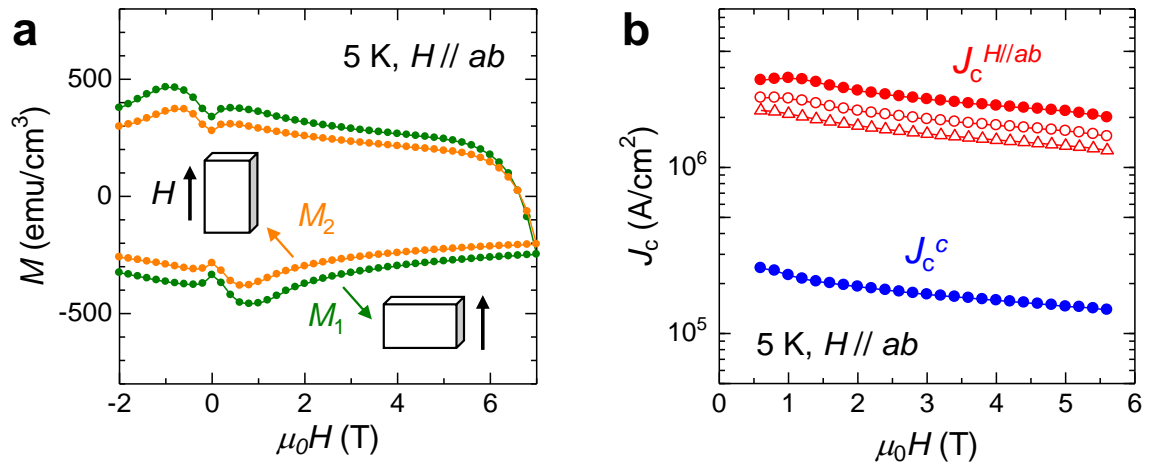


Fig. S8 Evaluation of $J_c^{H//ab}$ (red circles) and J_c^c for CaK1144. **a** MHLs for two setups (M_1 (green, $H // w$) and M_2 (orange, $H // l$)) at 5 K under $H // ab$. **b** H dependence of $J_c^{H//ab}$ (red circles) and J_c^c (blue circles) derived from M_1 and M_2 using the extended Bean's critical state model.^{3,4} The open circles and triangles are $J_c^{H//ab}$ values calculated using the simplified formula by taking $J_c^{H//ab} = J_c^c$ from each single MHL, M_1 and M_2 , respectively.

References

1. Meier, W. R., Kong, T., Bud'ko, S. L. & Canfield, P. C. Optimization of the crystal growth of the superconductor CaKFe₄As₄ from solution in the FeAs–CaFe₂As₂–KFe₂As₂ system. *Phys. Rev. Mater.* **1**, 013401 (2017).
2. van der Beek, C. J. *et al.* Quasiparticle Scattering Induced by Charge Doping of Iron-Pnictide Superconductors Probed by Collective Vortex Pinning. *Phys. Rev. Lett.* **105**, 267002 (2010).
3. Gyorgy, E. M., van Dover, R. B., Jackson, K. A., Schneemeyer, L. F. & Waszczak, J. V. Anisotropic critical currents in Ba₂YCu₃O₇ analyzed using an extended Bean model. *Appl. Phys. Lett.* **55**, 283 (1989).
4. Pyon, S. *et al.* Large and significantly anisotropic critical current density induced by planar defects in CaKFe₄As₄ single crystals. *Phys. Rev. B* **99**, 104506 (2019).